JOURNAL OF PROPULSION AND POWER
Vol. 20, No. 4, July–August 2004

Side-Load Phenomena in Highly Overexpanded Rocket Nozzles

Jan Östlund*
Volvo Aero Corporation, S-461 81 Trollhättan, Sweden,
Royal Institute of Technology, S-144 00 Stockholm, Sweden
and
Tomas Damgaard† and Manuel Frey‡
Volvo Aero Corporation, S-461 81 Trollhättan, Sweden

The operation of rocket engines in the overexpanded mode, that is, with the ambient pressure considerably higher than the nozzle exit wall pressure, can result in dangerous lateral loads acting on the nozzle. These loads occur as the boundary layer separates from the nozzle wall and the pressure distribution deviates from its usual axisymmetric shape. Different aerodynamic or even coupled aerodynamic/structural mechanic reasons can cause an asymmetric pressure distribution. A number of subscale tests have been performed, and three potential origins of side loads were observed and investigated, namely, the pressure fluctuations in the separation and recirculation zone due to the unsteadiness of the separation location, the transition of separation pattern between free-shock separation and restricted-shock separation, and aeroelastic coupling, which indeed cannot cause but do amply existing side loads to significant levels. All three mechanisms are described in detail, and methods are presented to calculate their magnitude and pressure ratio at which they occur.

Nomenclature

B	=	normalized pressure shift coefficient
C	=	separation point shift coefficient
F	=	force
F'	=	differential force
f	=	frequency
J	=	mass of inertia
k	=	stiffness
L, l	=	length
M	=	Mach number or torque
m	=	mass
$\boldsymbol{n}$	=	wall normal vector
p	=	pressure
q	=	nondimensional variable
r	=	radius
S	=	surface
s	=	arc length
t	=	time
t_1	=	pulse-duration time
u, v	=	velocity
$\boldsymbol{w}$	=	wall displacement
x	=	axial position
$\boldsymbol{x}$	=	vector of location
y	=	horizontal position
z	=	vertical position
γ	=	specific heat ratio
δ	=	boundary layer
δ^*	=	displacement thickness
ε	=	area ratio
θ	=	tilt angle
ρ	=	density
σ	=	rms value
τ	=	period time or wall angle
τ_w	=	wall friction
φ	=	azimuth
ψ	=	pressure shift coefficient
ω, Ω	=	angular frequency

Subscripts

a	=	aerodynamic or ambient
e	=	exit
ff	=	full flowing
i	=	interaction
m	=	measured or mechanical
max	=	maximum
n	=	natural
p	=	plateau
r	=	recirculating
s	=	separation
t	=	throat
w	=	wall
y	=	horizontal
0	=	undisturbed flow state or stagnation condition

Presented as Paper 2001-3684 at the Side load phenomena in highly overexpanded rocket nozzles, Joint Propulsion conference in Salt Lake City, 8 July 2001; received 11 June 2003; revision received 3 December 2003; accepted for publication 3 December 2003.

*Research Engineer, Engineering Department Nozzles, Space Propulsion Division; Ph.D. Student, Department of Mechanics; jan.ostlund@volvo.com.

†Research Engineer, Engineering Department Nozzles, Space Propulsion Division; tomas.damgaard@volvo.com.

‡Research Engineer, Engineering Department Nozzles, Space Propulsion Division; manuel.frey@volvo.com.

Introduction

THE performance of a rocket engine is strongly influenced by the characteristics and function of its nozzle extension. The characteristics of a conventional nozzle under vacuum conditions are well understood, and under this condition, design tools are available. However, during operation at highly overexpanded conditions, the rocket nozzle will be exposed to dynamic loads due to uncontrolled flow separation. These loads can sometimes be of such a magnitude that they present life-limiting constraints on thrust chamber components, as well as on the thrust vectoring control system.

The increasing demand for higher performance in rocket launchers promotes the development of nozzles with higher performance and, hence, larger area ratio. In a high area ratio nozzle, the flow will not be fully attached, but separated during testing at sea-level condition and during the first phase of the actual flight. In a nozzle

that is not full flowing, the separation line will move toward the nozzle exit when the chamber to ambient pressure ratio increases. Different kinds of dynamic loads occur in the nozzle when the flow is separated. The most well-known of these dynamic loads, which has received attention in the literature, is the so called side load. To avoid damage from these loads, a deeper understanding of the phenomena involved is needed.

A focused work dedicated to the investigation of the flow separation phenomena in rocket nozzles and corresponding side loads was initiated in 1997.[1] In the course of this work, numerous subscale tests were performed in the modified hypersonic wind tunnel HYP500 at the Aeronautical Research Institute of Sweden (FFA) (now a part of the Swedish Defence Research Agency) in Stockholm.[1–3] Heated air was used as driving gas to avoid condensation. Dynamic and static wall pressure measurements were performed together with schlieren video recording to characterize the flowfield. The subscale models consist mainly of two parts: one fixed part mounted to the downstream flange of the wind tunnel and one hinged part (Fig. 1). The hinged part is fastened by a cardan, permitting the nozzle to move in two directions (Fig. 2). The side-load torque is measured around the nozzle throat in the cardan by strain gauges located on the torsion springs, and this motion simulates the throat-bending mode of a real rocket nozzle. Each of the different nozzle concepts tested was equipped with a stiffener ring at the nozzle exit to receive approximately the same eigenfrequency in all of the nozzle concepts. An overview of the nozzles analyzed is shown in Fig. 3.

In the test campaigns, three main types of side loads have been observed due to 1) random pressure fluctuation, 2) transition of separation pattern, and 3) aeroelastic coupling. All three types are described and exemplified by test results together with analysis in this paper. A fourth type of side loads, which is due to the influence of the external flow, is not addressed here.

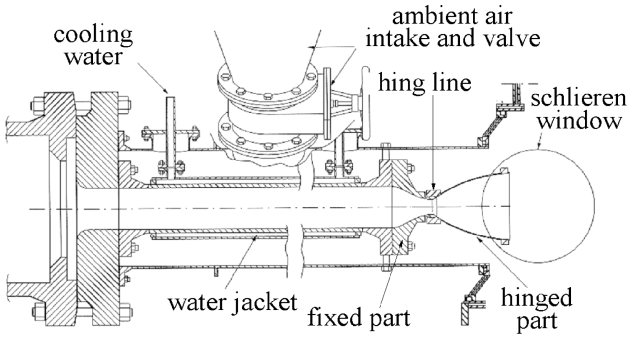

Fig. 1 Schematic side view of the cardan hinged test nozzle in FFA tunnel HYP 500.

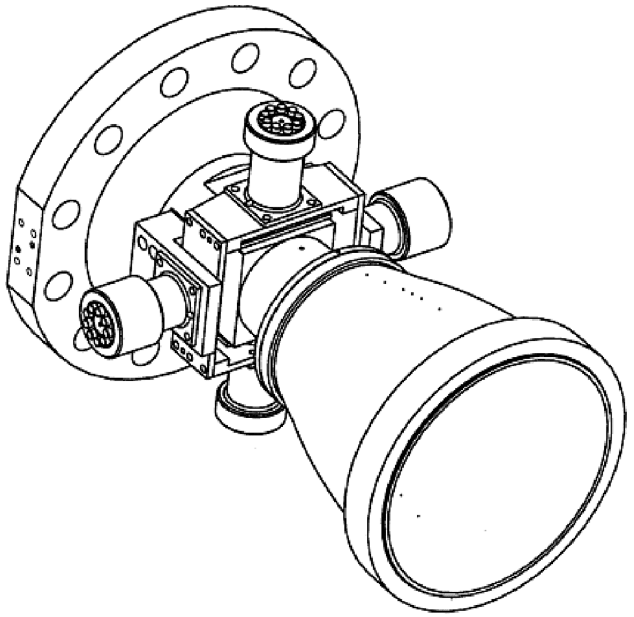

Fig. 2 Test nozzle with cardan suspension.

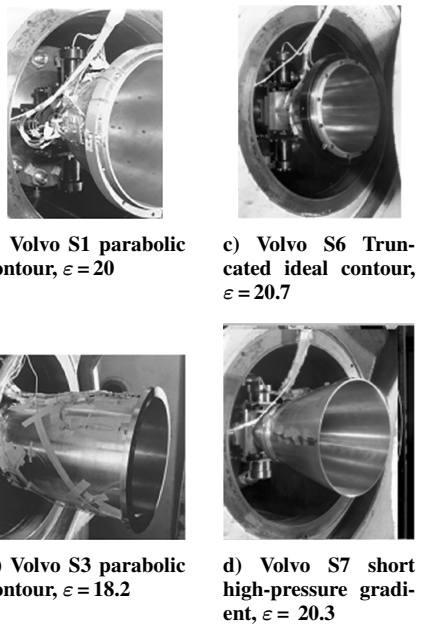

a) Volvo S1 parabolic contour, $\varepsilon = 20$

c) Volvo S6 Truncated ideal contour, $\varepsilon = 20.7$

b) Volvo S3 parabolic contour, $\varepsilon = 18.2$

d) Volvo S7 short high-pressure gradient, $\varepsilon = 20.3$

Fig. 3 Subscale nozzles tested by Volvo Aero Corporation (VAC) at FFA's HYP500 facility.

Side Loads Created by Random Pressure Fluctuations

Flow separation in supersonic flows is, of course, not limited to the field of rocket nozzles. When a supersonic flow meets a forward-facing step, a ramp, or an incident shock, the pressure rise in the boundary layer can be strong enough to cause flow separation. From basic experiments with exactly these configurations, it is known that the boundary-layer separation in turbulent supersonic flows is not a stationary process, even if the main flow is stationary.[4,5] Instead, the separation line and the shock resulting from the deflection of the flow show a highly instationary behavior, which seems to be triggered by the major scales of turbulence and also influences the recirculation region downstream.[6]

In rocket nozzles, basically the same phenomena can be observed. However, the separation location is not fixed by geometrical properties of the test configuration as in the earlier cases, but results mainly from the ratio of wall pressure to ambient pressure.

It is useful to describe the off-design condition as

$$n = p_{e,\mathrm{ff}}/p_a \tag{1}$$

where $p_{e,\mathrm{ff}}$ is the theoretic nozzle exit wall pressure for a full-flowing nozzle and p_a is the ambient pressure.

As an example, static wall pressure measurements from a truncated ideal nozzle (Volvo S6 in Fig. 3) are shown in Fig. 4. As expected, the separation point moves out of the nozzle when the off-design ratio n is increased towards unity, that is, the degree of overexpansion is reduced.

Based on the static wall pressure development, the flow can be divided in three regions. As shown in Fig. 5, upstream of the point of minimum static wall pressure (usually indexed i), the boundary layer is attached, and its behavior corresponds to a full-flowing nozzle. The following region of steep pressure rise, which ends at a certain plateau (often indexed p), is usually referred to as separation or interaction zone. In this region, the whole separation process take place, that is, thickening of boundary layer and physical flow separation (indexed s) at the zero wall friction point, $\tau_w = 0$. The last portion of the nozzle, where the flow is fully separated, shows a weak pressure rise until a wall pressure slightly below the ambient pressure is reached at the nozzle exit plane. This last portion is referred to as the recirculation zone.

When the dynamic behavior of the wall pressure is examined rather than the static behavior, interesting features of the flow can

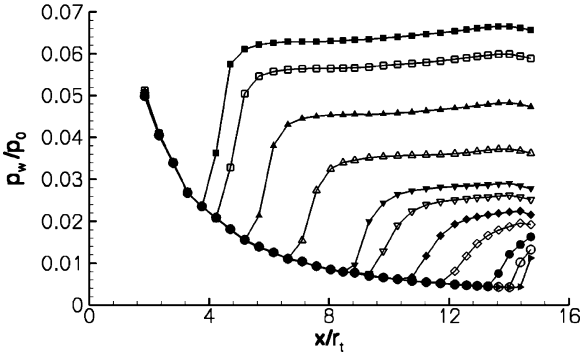

Fig. 4 Static wall pressure measurements in the S6 nozzle for different operational conditions, $n = 0.04$–0.24.

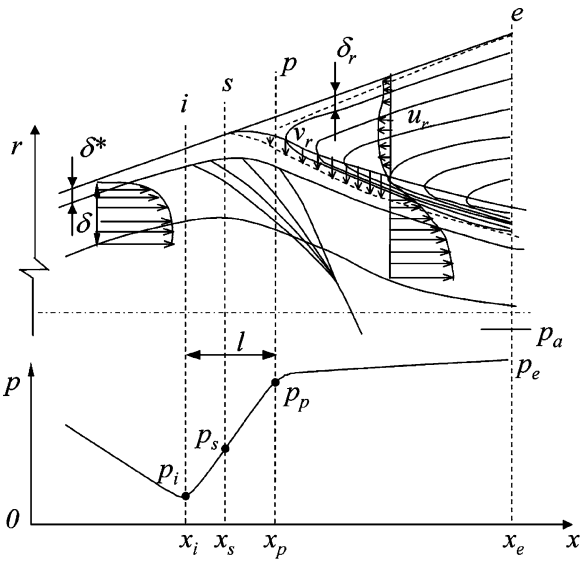

Fig. 5 Schematic of FSS.

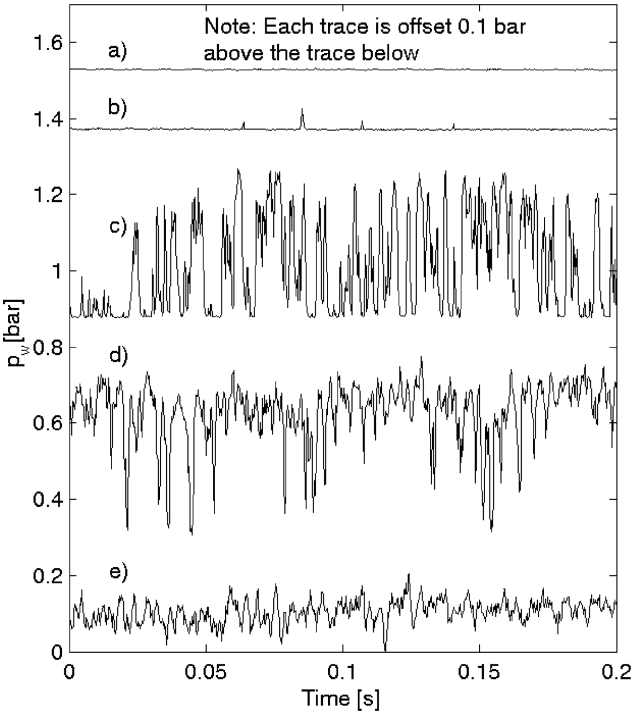

Fig. 6 Pressure signals at different positions through the separation zone in the Volvo S7 short nozzle; measurements made during down ramping of p_0.

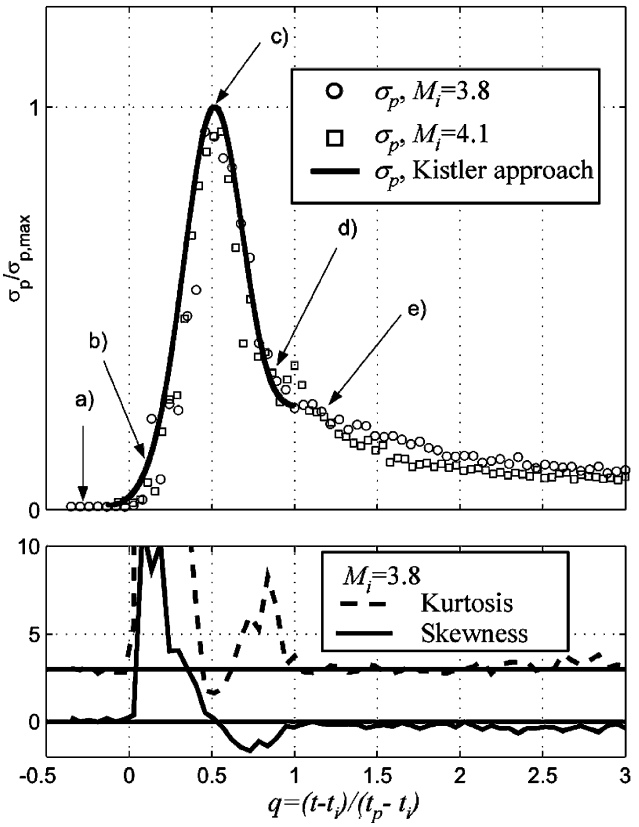

Fig. 7 Statistical evaluation of pressure signal at two different axial locations in the Volvo S7 short nozzle during down ramping of p_0: top, standard deviation values and bottom, skewness and kurtosis.

be observed. Figure 6 shows pressure signals in different parts of the separation zone, and Figure 7 shows the corresponding statistical moments. In Fig. 7, the axial positions correspond to $M = 3.8$ and $M = 4.1$ in the full-flowing nozzle. Each symbol is based on 800 samples collected during 0.2 s. The data were obtained at transient operation of the Volvo S7 short nozzle (Fig. 3). During down-ramping of the chamber pressure, the separation zone moves over the transducers during the time t_p–t_i, where the subscripts i and p refer to the start of the separation zone and the plateau point, respectively. Because the ramping is slow compared to the typical timescale of the pressure fluctuations, the variation of σ_p over time can be interpreted as the streamwise evolution by defining a nondimensional coordinate $q = (t - t_i)/(t_i - t_p)$. Figure 7 shows this behavior for two pressure transducers located at different axial positions. As can be seen, the two curves in Fig. 7 (representing the normalized standard deviation of the measured pressure signals) coincide, which proves that this generalization is valid. Outside the separation zone (signals a and e, Fig. 7), the pressure fluctuations follow a Gaussean distribution, with skewness near zero and the kurtosis equal to three. In contrast, the separation zone is characterized by high intermittency: at the beginning with a positive skewness (Fig. 7, signal c) and toward the end with a negative skewness (Fig. 7, signal d). In fact, the onset of high values of skewness and kurtosis (flatness) constitutes an accurate criterion for detecting the beginning and end of the separation zone.

The explanation of the obtained feature, first given by Kistler,[4] is that the flow is intermittent. In the separation zone, the pressure jumps back and forth between the mean pressure levels p_i and p_p due to a fluctuation of the separation point, and at each pressure level, the pressure oscillates with an amplitude characteristic of that level, that is, $\sigma_{p,i}$ and $\sigma_{p,p}$, respectively.

According to Kistler,[4] the wall pressure signal near the separation can be modeled as a step function, with the jump location, that is, the shock wave, moving over some restricted range. When ε is defined as the fraction of time that the plateau pressure region is acting over the point of interest, that is, an intermittence factor, the mean

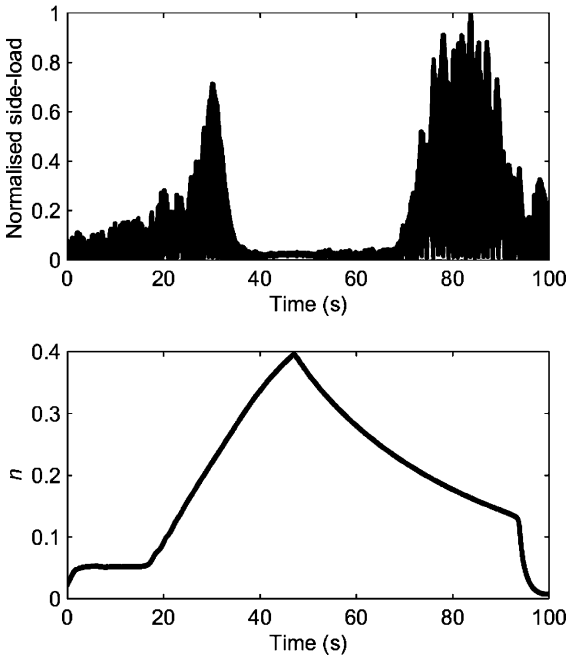

Fig. 8 Side loads created in a nozzle with random pressure pulsation.

pressure at a given axial position x can be expressed as

$$p(x) = \varepsilon(x)p_p + [1 - \varepsilon(x)]p_i \tag{2}$$

and the mean-square fluctuation around the mean pressure becomes

$$\sigma_p^2(x) = \overbrace{\underbrace{\varepsilon[1-\varepsilon](p_p - p_i)^2}_{\text{Low freq. part}}}^{\text{Shock motion}} + \overbrace{\underbrace{\varepsilon\sigma_{p,p}^2}_{\text{High freq. part}}}^{\text{Shear layer}} + \overbrace{\underbrace{[1-\varepsilon]\sigma_{p,i}^2}_{\text{High freq. part}}}^{\text{Boundary layer}} \tag{3}$$

Erengil and Dolling[7] showed, on the basis of ramp flow data, that the error function gives a good fit to the distribution of ε over the interaction region. This means that the position of the separation shock has a Gaussian distribution within this region.

The comparison in Fig. 7 with pressure rms values calculated with a refined Kistler approach (see Ref. 8) shows that the intermittence model gives correct results and can be applied to separated nozzle flows.

The pressure fluctuations have a random character, but show a clear correlation both in space and time. Therefore, they cause deviations from the axisymmetric flow and, hence, can produce forces perpendicular to the nozzle axis. Figure 8 shows those forces as a function of test time and operational condition for the Volvo S6 nozzle. Dumnov[9] presented a methodology to calculate the size of such forces based on the measurement of correlations both in time and space. This method is well suited to predict side loads in conical or truncated ideal nozzles.

Note that the earlier described side load, which results from random pressure fluctuations, is an aerodynamic force that acts on the dynamic system of the nozzle or the engine. To calculate the system response, that is, strains, deformations, and movements, it is necessary to solve a forced-response problem. The same holds true if the aerodynamic side load should be extracted from measurements: Because only the system response can be measured, a recalculation of the aerodynamic force is necessary, which requires the precise knowledge of the system's dynamic behavior. One possibility to do this is to determine the system's transfer function.[10] This procedure was also used to calculate the aerodynamic side loads from test data recorded at the HYP500 rig.

Side Loads Created by Transition of Separation Pattern

The classic, well-documented case of flow separation in nozzles is the free shock separation (FSS), where the flow continues as free-jet downstream of the separation point and does not reattach to the nozzle wall (Fig. 5). In nozzles with an internal shock that induces a cap shock pattern,[3] for example, compressed truncated ideal contours, parabolic contours, and directly optimized nozzles, a second separation pattern can occur. It is characterized by a reattachment of the separated flow to the nozzle wall and commonly referred to as restricted shock separation (RSS).[1,3,11,12] Two well-known full-scale nozzles where RSS occurs are the Vulcain and the space shuttle main engine (SSME) nozzle.

In the subscale testing, this behavior is detected in the parabolic nozzles Volvo S1 (Fig. 9) and Volvo S3. Numerical simulation was done using an in-house code that used the Menter[13] shear stress transport (SST) turbulence model. Figure 10 shows the side forces for the S1 nozzle, which are dominated by the changes in separation pattern.

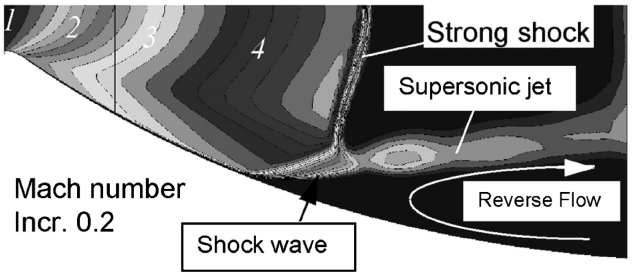

a) FSS at $n = 0.13$

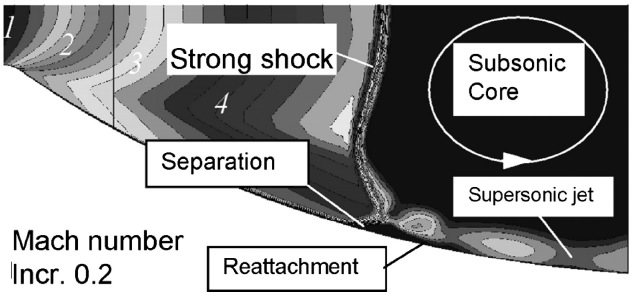

b) RSS at $n = 0.15$

Fig. 9 Volvo S1 nozzle at start-up.

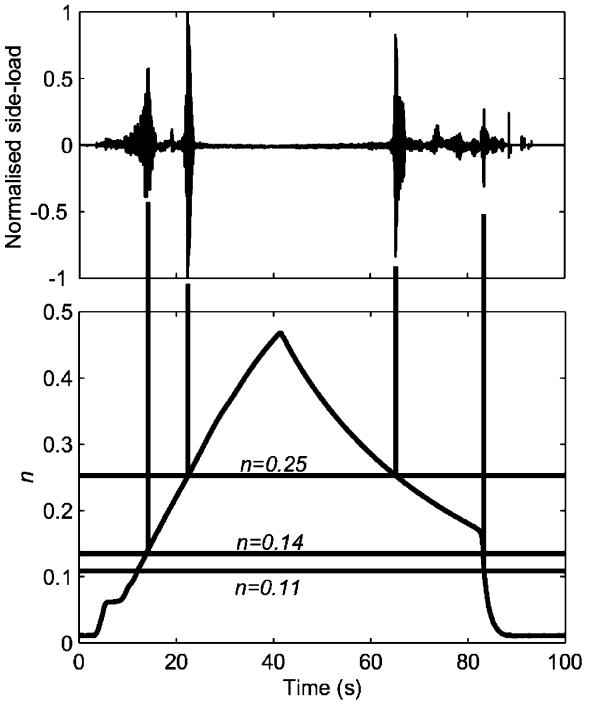

Fig. 10 Side loads created in the parabolic S1 nozzle due to transition in separation pattern.

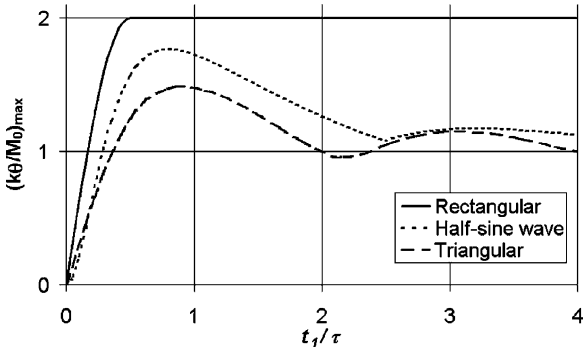

Fig. 11 SRS for different pulse shapes.

During startup, a transition from FSS to RSS occurs at an off-design ratio of $n = 0.14$ (Fig. 10). This rapid unsymmetrical transition creates a side-load impulse acting on the nozzle structure. Because of the short duration of the aerodynamic side load, the pulse excitation theory[10] can be used when evaluating the mechanical load. With this theory, the dynamic response factor, that is, the amplification of the applied load due to the dynamic system, is less than two for any single pulse. The most critical pulse is the single square wave because it contains the highest energy that any single pulse of defined strength and length can have. Figure 11 shows the shock response spectrum (SRS) for a single square wave together with the SRS for the half-sine wave and triangular pulse. The half-sine and the triangular pulse are often good approximations to real pulse shapes, for example, the load created by the aforementioned transition from FSS to RSS. If the transition time t_1 and the natural period of the mechanical eigenmode τ are known, the dynamic response factor can be obtained from Fig. 11.

The second side-load peak at $n = 0.25$ is created as the reattachment point reaches the nozzle exit and the closed separation bubble opens to ambient. The ambient pressure, which is higher than the pressure in the closed separation bubble, pushes the separation point upstream, which can result in a renewed reattachment of the flow to the wall and a downstream movement of the separation point. This process can recur periodically until the nozzle pressure ratio has been increased sufficiently and, thus, causes a continuously pulsating force on the nozzle. In contrast to the FSS–RSS transition side load described earlier, which was treated by the pulse excitation theory, the second peak should be treated as a forced response phenomenon. If the mechanical eigenfrequency of the system is close to the aerodynamic side-load frequency, it can lead to a severe side-load amplification and, thus, fatigue of mechanical components. The failure of an SSME fuel feed line was explained by this phenomenon.[14]

Different models have been proposed for the prediction of the aerodynamic load due to the transition between separation patterns (Hagemann et al.[11]). The basic idea in all proposed models is the same: It is assumed that the transition does not occur in a symmetric way. A worst-case assumption is that during this transition, one-half of the nozzle experiences free-shock separation while there is restricted-shock separation at the opposite half. Of course, the wall pressure distribution for the two different separation patterns is not the same; hence, a lateral force is produced. The side sload is then calculated from the momentum balance over the entire nozzle surface area. The key point for predicting the side-load level correctly is first to predict the operational condition where the transition from FSS to RSS takes place and second to calculate the corresponding FSS and RSS flow conditions. This can be done with computational fluid dynamics (CFD) or semi-empirical models or a combination of both (Hagemann et al.[11]).

Aeroelastic Stability

In highly aeroelastic cases, a significant amplification of the side load can occur as the flow interacts with the mechanical structure. The study of aeroelastic effects in separated nozzle flows is rather complex, requiring dynamic models of the mechanical nozzle–engine support system and the flow separation, as well as the coupling between these two. A technique for handling these difficult coupling problems was proposed by Pekkari[15,16] in the early 1990s. The model consists of two main parts, the first dealing with the equation of motion of the thrust chamber as aerodynamic loads are applied and a second part modeling the change of the aerodynamic loads due to the elastic deformation of the wall contour. In the original work by Pekkari, the pressure shift due to the deformation of the wall is determined by using the linearized supersonic flow theory. However, experience has shown that this theory significantly overpredicts the pressure shift when it is applied to internal nozzle flow, and therefore, a modified approach is proposed here, where the pressure shift is extracted from three-dimensional Euler simulations. This modified model predicts the aeroelastic stability and the modification of eigenfrequencies due to aeroelastic effects, as well as the transient behavior during startup and shutdown of the nozzle. Different mechanical eigenmodes can be treated, however, from side load point of view, the aeroelastic behavior of the bending mode is the most relevant one.

In the following section, the applied aeroelastic theory will be described, and results will be compared to the Volvo S1 and S6 cold-gas subscale tests (Fig. 3). Thanks to the simple test setup, the mechanical system can be described analytically (in contrast to real rocket engine cases, which require a complex finite element model analysis) and the basic model assumptions can, thus, be verified separately.

Geometry

The coordinate system implemented and the definition of the nozzle motion is shown in (Fig. 12).

The model nozzle is mounted on a flexible joint or cardan with stiffness k located at the throat. Here, θ is the tilt angle between the nozzle centerline and the combustion chamber centerline. L is the nozzle length from the throat to the exit, m the mass, and J_y the mass of inertia around the y axis. Also, τ is the local contour angle with respect to the nozzle centerline, and $r(x)$ is the local radius of the nozzle at the axial location x. Furthermore, $\boldsymbol{w}$ describes the displacement of the nozzle wall. The circumferential location is denoted by the angle φ, and p, M, u, ρ are the freestream flow properties along the wall.

Equation of Motion

Following the analysis of Pekkari,[15,16] the system is considered as quasi static with respect to the flow, that is, the characteristic

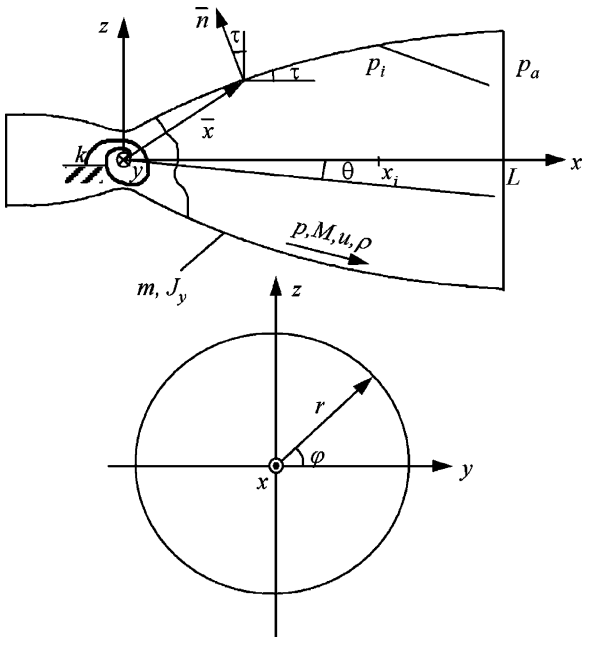

Fig. 12 Nozzle and flow separation geometry.

timescales of the flow are considered to be an order of magnitude faster than the characteristic timescales of the mechanical system.

In the y direction, the equation of motion for the bending of the nozzle by an angle θ, without considering damping, is

$$J_y\ddot{\theta} = M_m(\theta) + M_a(\theta) \tag{4}$$

M_m is the mechanical torque, that is, the restoring torque of the spring in the nozzle suspension,

$$M_m = -k\theta \tag{5}$$

and M_a is the y component of the aerodynamic torque induced by the pressure load onto the nozzle wall, neglecting any wall friction,

$$\boldsymbol{M}_a(\theta) = \iint \boldsymbol{x} \times \{p[\boldsymbol{w}(\theta), x] - p_a\} \cdot \boldsymbol{n}\, \mathrm{d}S \tag{6}$$

Here, $\boldsymbol{n}$ is the wall surface normal vector as indicated in Fig. 12, and $\boldsymbol{x}$ is the corresponding vector of location,

$$\boldsymbol{n} = \{-\sin\tau, \cos\tau\cos\varphi, \cos\tau\sin\varphi\} \tag{7}$$

$$\boldsymbol{x} = \{x, r(x)\cos\varphi, r(x)\sin\varphi\} \tag{8}$$

Eigenfrequency

The equation of motion for the mechanical system alone, that is, the nozzle without flow, is derived by putting the considered harmonic amplitude motion solution

$$\theta \sim e^{i\omega t} \tag{9}$$

into Eq. (4) and leaving out the aerodynamic torque M_a,

$$J_y\ddot{\theta} = M_m(\theta), \qquad -J_y\omega^2\theta = -k\theta \tag{10}$$

From Eq. (10), the eigenfrequency is found as

$$\omega^2 = k/J_y \tag{11}$$

This frequency can be found with hammer tests. Now, a nozzle with flow and, thus, with aerodynamic load M_a is considered, again assuming the motion to be purely harmonic,

$$\theta \sim e^{i\Omega t} \tag{12}$$

Introducing Eq. (12) in (4) and dividing by Eq. (11) gives

$$-J_y\Omega^2\theta = -k\theta + M_a, \qquad (\Omega/\omega)^2 = 1 - [M_a(\theta)/k\theta] \tag{13}$$

The analysis of Eq. (13) shows that, when $M_a/k\theta < 0$, the aeroelastic torque acts to restore the nozzle to its nominal position, that is, the system becomes stiffer than the mechanical structure itself and the frequency of the eigenmode is shifted to a higher frequency, that is, $(\Omega/\omega)^2 > 1$.

The analysis of Eq. (13) also shows that, when $M_a/k\theta \in [0, 1]$, the aeroelastic torque acts in the same direction as the displacement of the nozzle wall, that is, the system becomes weaker than the mechanical structure itself and the frequency of the eigenmode is shifted to a lower frequency, that is, $(\Omega/\omega)^2 \in [0, 1]$.

Finally, analysis of Eq. (13) shows that, when $M_a/k\theta > 1$, the unconditionally stable eigenmode becomes aeroelastically unstable, that is, $(\Omega/\omega)^2 < 0$, and the displacement of the nozzle will start to grow exponentially.

Aerodynamic Load

To calculate the aerodynamic load and the associated frequency shift, the wall pressure distribution of the deformed nozzle must be known. As in the original model by Pekkari,[15,16] the pressure upstream of the separation point x_i is assumed to be the pressure of the attached boundary layer, but taking into account the asymmetric deformation. Downstream of the separation point, a pressure recovery occurs, and the pressure gradually approaches the ambient pressure. However, the model presented here assumes this pressure to be equal to the ambient pressure p_a for simplicity and clarity,

$$p(\boldsymbol{w}, \boldsymbol{x}) = \begin{cases} p(x) + p_0\Psi(\boldsymbol{w}, \boldsymbol{x}), & x \le x_i \\ p_a, & x > x_i \end{cases} \tag{14}$$

Here $p(x)$ is the axisymmetric wall pressure in the undeformed nozzle. The second term in the pressure upstream of the separation line is the disturbance of the wall pressure due to the deformation of the nozzle contour, that is,

$$\Psi(\boldsymbol{w}, \boldsymbol{x}) = [p(\boldsymbol{w}, \boldsymbol{x}) - p(x)]/p_0 \tag{15}$$

where p_0 is the stagnation pressure.

The location of the separation point is considered to be given by a separation criterion of Summerfield type:

$$p_i/p_a = \text{const} \tag{16}$$

In the original work by Pekkari, the pressure shift, ψ, was calculated with the use of the small perturbation theory (SPT), that is,

$$\Psi(\boldsymbol{w}, \boldsymbol{x}) = \frac{\rho u^2}{p_0\sqrt{M^2 - 1}}\frac{\partial w}{\partial s} = B\frac{\partial w}{\partial s} \tag{17}$$

Here $w = \boldsymbol{w} \cdot \boldsymbol{n}$ is the normal displacement of the nozzle wall surface and s is the arc length along the wall in the axial direction; thus, for small deflections, $\partial w/\partial s$ is the angle of deformation. B is the normalized pressure shift coefficient, which expresses the change in pressure with the wall deformation. However, experience has shown that SPT overpredicts the pressure shift in deformed nozzles. Therefore, a modified approach is proposed,[3] where the normalized pressure shift coefficient B is extracted from three-dimensional Euler simulations:

$$B(x) = \frac{\Psi(\boldsymbol{w}, \boldsymbol{x})}{\partial w/\partial s} = \frac{p(\boldsymbol{w}, \boldsymbol{x}) - p(x)}{p_0\partial w/\partial s} \tag{18}$$

A test was performed where the S1 nozzle was statically deformed by 1 deg to verify the simulation results. In Fig. 13, the measured and the calculated wall pressure profile are shown for the undeformed and deformed S1 nozzle, respectively. As can be seen in

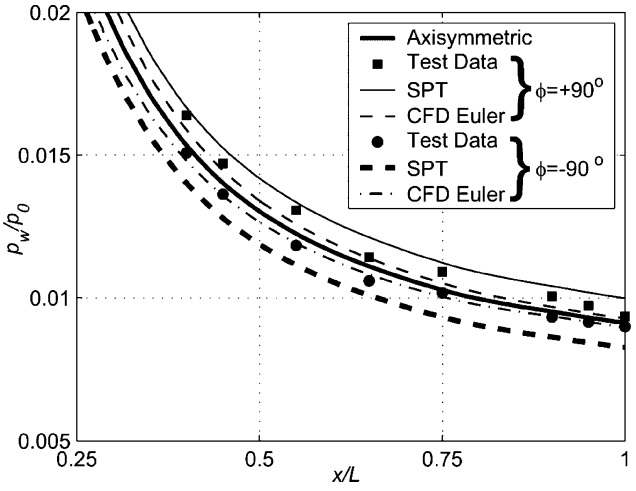

Fig. 13 Measured and calculated wall pressure in the S1 nozzle statically deflected by 1 deg.

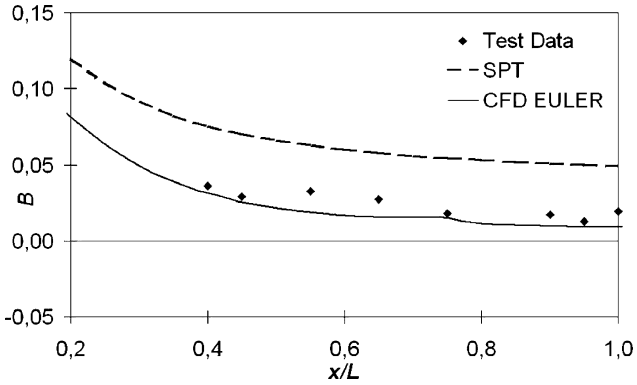

Fig. 14 Comparison between calculated and measured normalized pressure shift coefficient B in the S1 nozzle.

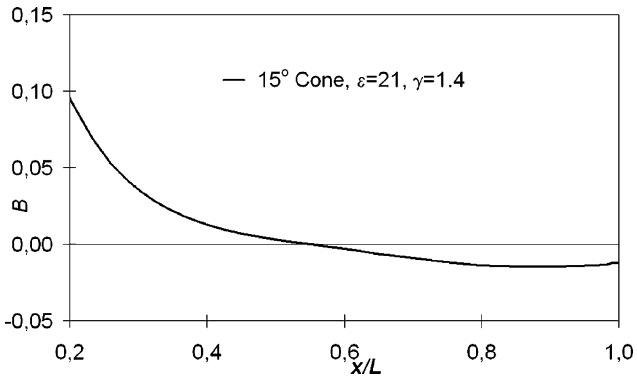

Fig. 15 Normalized pressure shift coefficient in conical nozzle.

Fig. 13, there is good agreement between the CFD prediction and the measured wall pressure, whereas SPT overpredicts the pressure shift considerably.

This effect can be seen even more clearly in Fig. 14, which shows the corresponding normalized pressure shift coefficient B. The SPT method overpredicts the pressure shift coefficient by approximately a factor of four for this case. The CFD predictions, on the other hand, show close agreement with the experimental data and, thus, validate the use of Euler simulations for calculating the pressure shift coefficient.

Note that the deviation of the wall pressure due to bending around the throat is highly dependent on the nozzle contour itself. As shown in Refs. 12 and 17, the secondary flow effects due to the uneven flow distribution around the circumference in a conical nozzle are so strong that the pressure deviation trend even reverses itself: On the side with higher flow angles, where more expansion is expected, the wall pressure in some portions of the nozzle is even higher than on the opposite side. This finding has been confirmed by our own numerical simulations and underscores the necessity of case-sensitive methods. See Fig. 15 and note the negative value of B.

A simple relation can be found by linearizing the aerodynamic torque around the initial location of the separation line in the undeformed nozzle, x_{i0}. Expanding the wall pressure for attached flow around x_{i0} gives

$$p(x_i) = p(x_{i0}) + \frac{\mathrm{d}p}{\mathrm{d}x}(x_i - x_{i0}) + \cdots \tag{19}$$

Equation (14) written at the axial station x_i is

$$p(\boldsymbol{w}, \boldsymbol{x}) = p(x) + p_0 B \left.\frac{\partial w}{\partial s}\right|_{x=x_i} \tag{20}$$

The separation pressure $p(\boldsymbol{w}, \boldsymbol{x})$ at $x = x_i$, approximated for the deformed wall contour by Eq. (20), will be the same as the separation pressure $p(x_{i0})$ for the undeformed wall contour included in Eq. (19). The separation line is, therefore, defined by

$$p(x_{i0}) = p(\boldsymbol{w}, \boldsymbol{x})|_{x=x_i} \tag{21}$$

which gives

$$p(x_i) - \frac{\mathrm{d}p}{\mathrm{d}x}(x_i - x_{i0}) = p(x_i) + p_0 B \left.\frac{\partial w}{\partial s}\right|_{x=x_i}$$

$$x_i - x_{i0} = \left[B \Big/ -\frac{\mathrm{d}}{\mathrm{d}x}\frac{p(x)}{p_0} \right] \left.\frac{\partial w}{\partial s}\right|_{x=x_i} = C \left.\frac{\partial w}{\partial s}\right|_{x=x_i} \tag{22}$$

where

$$C = B \Big/ -\frac{\mathrm{d}}{\mathrm{d}x}\frac{p(x)}{p_0}$$

which expresses the change of the separation point with the nozzle wall deformation.

The differential aerodynamic pressure force per circumferential fraction due to a small wall displacement may be written as

$$\mathrm{d}\boldsymbol{F}'_a(\boldsymbol{w}) = \boldsymbol{n}(p_i - p_a)(x_i - x_{i0}) r\,\mathrm{d}\varphi = \boldsymbol{n}(p_i - p_a) C \frac{\partial w}{\partial s} r\,\mathrm{d}\varphi \tag{23}$$

When the differential force is integrated along the separation line around the circumference, the aerodynamic pressure force is

$$\boldsymbol{F}_a(\boldsymbol{w}) = \oint_{l_{\mathrm{sep}}} \boldsymbol{F}'_a\,\mathrm{d}l = (p_i - p_a) \oint_{l_{\mathrm{sep}}} \boldsymbol{n} C \frac{\partial w}{\partial s}\,\mathrm{d}l \Bigg|_{x=x_{i0}} \tag{24}$$

The corresponding aerodynamic torque is

$$\boldsymbol{M}_a(\boldsymbol{w}) = (p_i - p_a) \oint_{l_{\mathrm{sep}}} \boldsymbol{x} \times \boldsymbol{n} C \frac{\partial w}{\partial s}\,\mathrm{d}l \Bigg|_{x=x_{i0}} \tag{25}$$

The change of the nozzle wall slope at different circumferential locations φ due to a small tilt angle θ of the nozzle can be expressed as

$$\frac{\partial w}{\partial s} \approx \theta \sin\varphi \tag{26}$$

When this and

$$\oint_{l_{\mathrm{sep}}} \ldots \mathrm{d}l \approx \int_0^{2\pi} \ldots r(x_{i0})\,\mathrm{d}\varphi \tag{27}$$

are used for small wall deformations, the aerodynamic torque can be expressed as

$$\boldsymbol{M}_a(\theta) \approx \{0, M_a, 0\}$$

$$M_a(\theta) = (p_a - p_i)\, C r \pi (x \cos\tau + r \sin\tau)\theta|_{x=x_{i0}} \tag{28}$$

When Eq. (28) is substituted in Eq. (13), the frequency shift, linearized around the initial location of the separation line, is obtained as

$$(\Omega/\omega)^2 = 1 - [(p_a - p_i) C r \pi (x \cos\tau + r \sin\tau)/k]|_{x=x_{i0}} \tag{29}$$

Typical Model Results

The general features of the aeroelastic model are best visualized by applying it to the Volvo S1 test case. The resulting natural oscillating frequencies of the bending mode are listed in Table 1 for the different spring setups used. The frequencies were determined by performing a ping test on the test article in the test facility. A more detailed description of the test program is presented in Ref. 1.

With the use of Eq. (29), the aeroelastic stability of the S1 nozzle can be calculated for the different spring setups. Such a calculation is presented in Fig. 16, with $p_i/p_a = 0.25$ and B from an Euler calculation according to Fig. 4. It can be seen that the only aeroelastically unstable system is the S1 nozzle with the superweak spring for $x_i/L > 0.8$.

The aeroelastically stable system will almost behave like a regular forced response system, that is, the closer the mechanical eigenfrequencies are to the frequencies of the aerodynamic load, the higher the generated loads. The exception is that a small shift of the system eigenfrequency and a corresponding small amplification of the forced response load will occur. The frequency shift and the size of the aeroelastic side-load amplification depend on the degree of coupling. For the weak, medium, stiff, and rigid spring setups considered here, the coupling is weak and the aeroelastic effect can almost be neglected.

For the aeroelastically unstable system, on the other hand, a significantly higher side-load magnitude can be expected compared to the classic forced response theory due to the aeroelastic instability. When the separation enters the section of the nozzle that is unstable, the displacement of the nozzle will start to grow exponentially. At the same time, the separation line will be displaced accordingly. The nonlinear growth of the nozzle displacement will saturate as parts of the separation line start to move out of the nozzle, that is, parts of the nozzle becomes full flowing, when the displacement becomes sufficiently high. This can be seen in the nonlinear stability relation (13), shown in Fig. 17 for tilt angles $\theta = 0.1$ and $\theta = 2.6$ deg. For comparison, the linearized stability relation (29) is also included in Fig. 17.

If we study the nonlinear stability relation for the S1 nozzle more carefully (Fig. 17), we can see that the aeroelastic instability occurs at $n = 0.25$. When n is increased further, the nozzle will become full flowing at $n \approx 0.27$, and the system becomes stiffer than the mechanical structure itself, that is, $(\Omega/\omega)^2 > 1$, because the aerodynamic torque now acts to stabilize the nozzle.

Table 1 Resulting natural oscillating frequencies of the bending mode for the different spring setups with the Volvo S1 nozzle

Spring	Natural frequency, H_2
Superweak	25.2
Weak	36.3
Medium	45.0
Stiff	57.5
Rigid	120

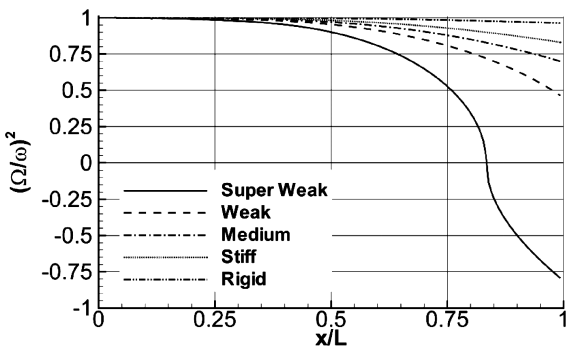

Fig. 16 Aeroelastic stability of the S1 nozzle for the different spring setups.

Table 2 Measured side-load magnitude vs frequency ratio between exciting load and mechanical system, peak at $n = 0.24$

Spring	ω_a/ω_n	$M/M_{\max}$
Rigid	0.8	0.66
Stiff	1.7	0.63
Medium	2.2	0.48
Weak	2.8	0.45
Superweak	3.9	1

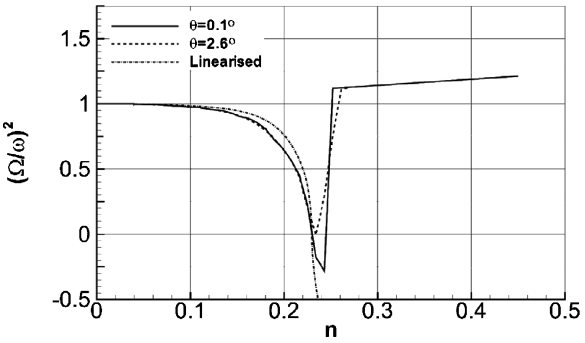

Fig. 17 Aeroelastic stability relation for the S1 nozzle hinged with the superweak spring.

Comparison with Experimental Data

In the following text, the presented model for the prediction of aeroelastic effects will be validated with respect to amplitude and frequency by comparing the model results to experimental data for the Volvo S1 nozzle and the Volvo S6 nozzle, respectively.

Volvo S1 Nozzle

Table 2 shows the measured side load at $n = 0.24$, obtained with the different spring setups. Schlieren videos show that the side load at this pressure ratio is connected to an oscillation of the whole separation shock system with a frequency of about $f_a = 100$ Hz ($\omega_a = 2\pi f_a$) near the nozzle exit.[3] When the aeroelastically stable systems (rigid to weak spring) are examined, the measured load decreases with decreasing spring stiffness, which can be explained by the classic forced response theory: The highest response is reached with the system's eigenfrequency f_n ($\omega_n = 2\pi f_n$) closest to the exciting frequency. However, the trend of decreasing response with increasing distance from the exciting frequency is clearly interrupted for the superweak spring. This behavior can be explained by aeroelastic amplification, and indeed, aeroelastic instability was predicted for the S1 nozzle with the superweak string in the preceding paragraph.

Volvo S6 Nozzle

In Fig. 18 the predicted frequency shift in the S6 nozzle is compared to experimental data. The experimental frequency shift of the eigenmode has been determined by applying the Welch method[18] for power spectral analysis on the measured steady-state side load at different constant pressure ratios. The sampling time was at least 8 s for each case to achieve sufficient frequency resolution. The frequency shift [Eq. (13)] for the S6 nozzle has been calculated with a tilt angle $\theta = 0.1$ deg, $p_i/p_a = 0.2$, and B extracted from an Euler calculation.

As indicated in Fig. 18, the theory predicts almost the same frequency shift as observed in experiments. The discrepancy is mainly due to the fact that both structural and gasdynamic damping was neglected in this analysis. Inclusion of damping in the analysis would increase the frequency shift, and the prediction should move closer to experimental data. However, the influence of the damping is only significant during steady-state operation, whereas during short

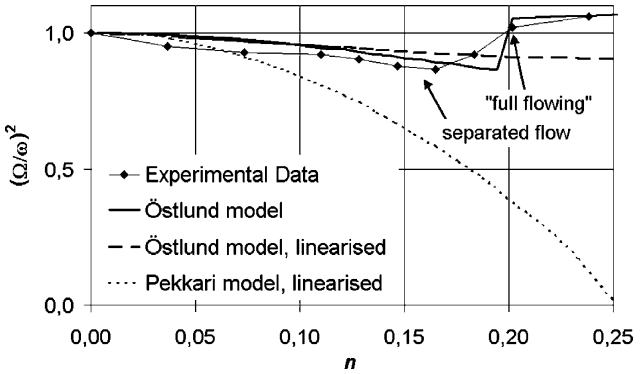

Fig. 18 Comparison between measured and calculated frequency shift for S6 nozzle.

transient phases, such as a rocket engine startup, the damping plays a minor role. Because damping plays a minor role, the simplification in the analysis becomes more valid.

Because of the simple separation model used, the sudden increase of the frequency is predicted somewhat later compared to experimental data. The gradient of the predicted frequency shift is also steeper compared with the experimental data. However, this is only a reflection of the single and very small tilt angle ($\theta = 0.1$ deg) used for calculating the frequency shift. In Fig. 17, it can be seen that the predicted gradient will be reduced for larger tilt angles. The increased system frequency observed in the experiments, when the nozzle becomes full flowing, is also well captured with the model.

In Fig. 18, the linearized frequency shift [Eq. (29)] calculated with the Östlund[3] and Pekkari[15] approaches are also shown to visualize how the frequency shift is overpredicted when determining B with SPT [cf. Eqs. (17 and 18)].

Pekkari[15,16] concluded in his work that the aeroelastic model results were qualitatively as well as quantitatively consistent with Vulcain side-load test results. As shown earlier, the aeroelastic coupling in the bending mode is not as strong as Pekkari anticipated. Today, we know that the high Vulcain side loads are caused by a transition between different separation patterns and not due to an aeroelastic phenomenon. Nevertheless, the experimental data as well as the modified model presented in this work show that aeroelastic effects can amplify the original side load and that the aeroelastic amplification is significant in weak nozzle structures. It has also been shown that the aeroelastic amplification is highly dependent on the nozzle contour.

The current work has only focused on aeroelastic effects coupled to the side-load phenomenon and not on possible aeroelastic instability of nozzle shell buckling modes. In recent tests of a flexible thin-walled ideal nozzle, Brown et al. found indications of a self-excited vibration loop coupling the ovalization mode to the flow separation.[19] So far, the mechanism for the observed response has not been clarified, and Brown et al. suggest that the lines laid down by Pekkari[15,16] should be followed.

Conclusions

Side-load phenomena in highly overexpanded rocket nozzles have been investigated with the help of extensive subscale testing at FFA. The starting point for side-load analysis is a deep understanding of the flow separation behavior in a rocket nozzle. Three different kinds of side loads have been analyzed.

The first kind of side loads analyzed are those created by random pressure fluctuations. When the pressure rise in the boundary layer is strong enough, the flow separates from the nozzle wall. This kind of flow separation can be seen in several basic flow experiments, for example, where a supersonic flow meets a forward-facing step. It can be seen that the boundary-layer separation in turbulent supersonic flows is not a stationary process, even if the main flow is stationary. Both the static and dynamic wall pressure behaviors have been studied. It has been shown in this paper that the behavior of the dynamic wall pressure constitutes a suitable criterion for detecting the beginning and end of the separation zone by analyzing the skewness and the kurtosis of its distribution. Furthermore, an error function approach was used for the prediction of pressure fluctuations in the separation zone.

The second kind of side loads analyzed are those created by transition of separation pattern. In nozzles with an internal shock that induces a cap shock pattern,[3] for example, compressed truncated ideal contours, parabolic contours, and directly optimized nozzles, a second separation pattern can occur. It is characterized by a reattachment of the separated flow to the nozzle wall and commonly referred to as RSS.[1–3,11,12] In the subscale test program performed, RSS was observed in the parabolic nozzles S1 and S3.

It is the rapid unsymmetrical transition that creates a side-load impulse acting on the nozzle structure. Because of the short duration of the aerodynamic side load, the pulse excitation theory[10] has been used when evaluating the mechanical load.

The third kind of side loads analyzed are those created by aeroelastic coupling. The model proposed by Pekkari[15,16] in the early 1990s has been analyzed and modified. Three-dimensional Euler simulations have been used, instead of small perturbation theory, when calculating the normalized pressure shift in a deflected nozzle. These new simulations have been compared with subscale test results of the deflected S1 and S6 nozzle and found to have good agreement. It has also been shown that the aeroelastic coupling can be significant in weak nozzle structures.

Acknowledgments

This work was funded by the Swedish National Space Board (SNSB) in the framework of the European Flow Separation Control Device (FSCD) program. The authors wish to thank SNSB for the funding and the members of the FSCD group for the fruitful technical discussions. Furthermore, special thanks are also extended to Lars Torngren and Johan Agrell at the Aeronautical Research Institute of Sweden for their excellent work with the experimental setup, manufacturing, and testing of the subscale nozzles.

References

[1]Mattsson (Östlund), J., Högman, U., and Torngren, L., "A Sub-scale Test Program on Investigation of Flow Separation and Side Loads in Rocket Nozzles," *Proceedings of the Third European Symposium on Aerothermodynamics for Space Vehicles*, ESA-SP-426, ESTEC, Noordwijk, Dec. 1998, pp. 373–378.

[2]Östlund, J., and Bigert, M., "A Subscale Investigation on Side-Loads in Sea Level Rocket Nozzles," AIAA Paper 99-2759, June 1999.

[3]Östlund, J., "Flow Processes in Rocket Engine Nozzles with Focus on Flow Separation and Side-Loads," Ph.D. Dissertation TRITA-MEK 2002:09, Dept. of Mechanics, Royal Inst. of Technology, Stockholm, May 2002.

[4]Kistler, A., "Fluctuating Wall Pressure under a Separated Supersonic Flow," *Journal of the Acoustical Society of America*, Vol. 36, No. 3, 1964, pp. 543–550.

[5]Coe, C., Chyu, W., and Dods, J., "Pressure Fluctuations Underlying Attached and Separated Supersonic Turbulent Boundary Layers and Shock Waves," AIAA Paper 73-996, Oct. 1973.

[6]Adams, N. A., "Direct Simulation of the Turbulent Boundary Layer Along a Compression Ramp at M = 3 and Re = 1685," *Journal of Fluid Mechanics*, Vol. 420, 2000, pp. 47–83.

[7]Erengil, M. E., and Dolling, D. S., "Correlation of Separation Shock Motion with Pressure Fluctuations in the Incoming Boundary Layer," *AIAA Journal*, Vol. 29, No. 11, 1991, pp. 1868–1877.

[8]Barter, J. W., and Dolling, D. S., "Prediction of Fluctuating Pressure Loads Produced by Shock-Induced Turbulent Boundary Layer Separation," AIAA Paper 96-2043, June 1996.

[9]Dumnov, G. E., "Unsteady Side-Loads Acting on the Nozzle with Developed Separation Zone," AIAA Paper 96-3220, July 1996.

[10]Harris, C. M., and Crede, C. E., *Shock and Vibration Handbook*, McGraw–Hill, New York, 1976.

[11]Hagemann, G., Terhardt, M., Frey, M., Reijasse, P., Onofri, M., Nasuti, F., and Östlund J., "Flow Separation and Side-Loads in Rocket Nozzles," 4th International Symposium on Liquid Space Propulsion, Rept. A620393, German Aerospace Center, Lampoldshausen, March 2000.

[12]Frey, M., "Behandlung von Strömungsproblemen in Raketendüsen bei Überexpansion," Ph.D. Dissertation, Dept. of Luft- und Raumfahrttechnik, Univ. of Stuttgart, Stuttgart, Germany, April 2001, http://elib.uni-stuttgart.de/opus/volltexte/2001/800 [cited 11 April 2001].

[13]Menter, F. R., "Zonal Two Equation k–ω Turbulence Models for Aerodynamic Flows," AIAA Paper 93-2906, July 1993.

[14]Larson, E. W., Ratekin, G. H., and O'Connor, G. M., "Structural Response of the SSME Fuel Feedline to Unsteady Shock Oscillations," 52nd Shock and Vibration Symposium, The Defence Nuclear Agency, The U.S. Army Waterways Experimental Station, The Shock and Vibration Bulletin, No. 52, Pt. 2, The Shock and Vibration Information Center Naval Research Lab., Washington, DC, May 1982, pp. 177–182.

[15]Pekkari, L.-O., "Aeroelastic Stability of Supersonic Nozzles with Separated Flow," AIAA Paper 93-2588, June 1993.

[16]Pekkari, L.-O., "Aeroelastic Analysis of Side-Loads in Supersonic Nozzles with Separated Flow," AIAA Paper 94-3377, June 1994.

[17]Kwan, W., "Aeroelastic Effects on a Bended Conical Nozzle," German Aerospace Research Center, DLR, Internal Rept. DLR-IB 645-2001-06, Lampoldshausen, June 2001.

[18]Welch, P. D., "The Use of Fast Fourier Transform for the Estimation of Power Spectra: A Method Based on Time Averaging over Short, Modified Periodograms," *IEEE Transactions on Audio Electroacoustic*, Vol. AU-15, June 1967, pp. 70–73.

[19]Brown, A. M., Ruf, J., Reed, D., and D'Agostino, M., "Characterization of Side Load Phenomena Using Measurement of Fluid/Structure Interaction," AIAA Paper 2002-3999, July 2002.